



**HAL**  
open science

## Sea surface temperature variability in the North Western Mediterranean Sea (Gulf of Lion) during the Common Era

Marie-Alexandrine Sicre, Bassem Jalali, Belen Martrat, Sabine Schmidt,  
Maria-Angela Bassetti, Nejb Kallel

► **To cite this version:**

Marie-Alexandrine Sicre, Bassem Jalali, Belen Martrat, Sabine Schmidt, Maria-Angela Bassetti, et al. Sea surface temperature variability in the North Western Mediterranean Sea (Gulf of Lion) during the Common Era. *Earth and Planetary Science Letters*, 2016, 456, pp.124-133. 10.1016/j.epsl.2016.09.032 . hal-01386646

**HAL Id: hal-01386646**

**<https://hal.sorbonne-universite.fr/hal-01386646>**

Submitted on 24 Oct 2016

**HAL** is a multi-disciplinary open access archive for the deposit and dissemination of scientific research documents, whether they are published or not. The documents may come from teaching and research institutions in France or abroad, or from public or private research centers.

L'archive ouverte pluridisciplinaire **HAL**, est destinée au dépôt et à la diffusion de documents scientifiques de niveau recherche, publiés ou non, émanant des établissements d'enseignement et de recherche français ou étrangers, des laboratoires publics ou privés.



## 30 **1. Introduction**

31 In the past decade, major efforts have been done to document the multi-decadal variability of  
32 the sea surface temperatures during the Common Era (last 2,000 yr) and to explore the role of  
33 external forcings (solar, volcanism, greenhouse gases) by combining paleo records and  
34 numerical simulations of the last millennium climate (McGregor et al., 2015; Sicre et al.,  
35 2011). Although the number of pre-instrumental reconstructions of sea surface temperature  
36 (SST) resolving the decadal scale has increased significantly they are still insufficient to  
37 precisely describe the space-time climate variability both at global and regional scales. This is  
38 particularly true for the Mediterranean region for which very few records exist despite  
39 alarming future climate projections (Lionello et al., 2006). Indeed, the Mediterranean region  
40 is one of the most sensitive areas to climate change owing to its geographical location  
41 between the temperate climate of Europe and the arid climate of North Africa. Because of  
42 this, even minor modifications in the extension and intensity of these climate zones can  
43 substantially alter the Mediterranean climate making this region particularly vulnerable to  
44 global warming (Lionello et al., 2006). In its history, the Mediterranean region has undergone  
45 important changes that can be investigated to better understand present-day interactions  
46 between global and regional climate and the underlying driving mechanisms.

47 The Mediterranean climate is strongly influenced by the large-scale mid-latitude atmospheric  
48 circulation of the North Atlantic (NA) and primarily the East Atlantic pattern (EA) and the  
49 North Atlantic Oscillation (NAO; Hurrell, 1995). The NAO, the dominant mode of  
50 atmospheric variability in the NA, reflects the atmospheric pressure difference between the  
51 Azores High and Icelandic low. The NAO state determines the latitudinal position of the NA  
52 storm tracks driving the Mediterranean winter precipitation, but its role on Mediterranean  
53 SSTs is secondary (Lionello et al., 2006). Instead, the EA has been recently recognized as the  
54 main controlling factor of the SST variability of the Mediterranean Sea, particularly in the  
55 western basin (Josey et al., 2011). The EA mode has a similar North South dipole structure as  
56 the NAO but its centers of action are displaced southeastward, which results in a stronger link

57 with the subtropical climate than NAO. Teleconnections with El Nino Southern Oscillation  
58 (ENSO) have also been suggested mainly to explain winter rainfall in some areas of the  
59 Mediterranean region (Alpert et al., 2006). Finally, the influence of the Atlantic Multidecadal  
60 variability (AMV) (Knight et al., 2006) has been recently pointed out, yet the dynamical links  
61 between AMV and Mediterranean SSTs is still an open question. Indeed, oceanic processes  
62 have been suggested based on the detection of AMV-like 70-yr period oscillations in the  
63 Mediterranean SSTs (Marullo et al., 2011) while according to the study of Mariotti and  
64 Dell'Aquila (2012) atmospheric transmission of AMV is more likely.

65 The complex topography of the Mediterranean basin modifies the large-scale atmospheric  
66 flow and subsequently influences the climate characteristics at a local scale. In the  
67 northwestern Mediterranean Gulf of Lion (GoL), interactions between the mid-latitude  
68 westerly winds and the Alps result in northerly winds blowing offshore in the South of  
69 France, called Mistral (Jiang et al., 2003). This cold and dry wind blows at all seasons  
70 (climatologically 49% of wind frequency is in the northwest quadrant; Burlando, 2009), but  
71 more strongly in winter and spring (Jiang et al, 2003) causing intense surface water cooling.  
72 Najac et al. (2009) have shown that Mistral is favored by anticyclonic blocking over the  
73 northeastern Atlantic and a low-pressure system in the central Mediterranean Sea (Fig. 1), a  
74 synoptic configuration described by negative EA that focuses the northerly air flow over  
75 France. Despite previous suggestions of a dynamical connection between negative NAO and  
76 the occurrence of NA blocking (Shabbar et al., 2001), the most severe Mistral episodes show  
77 only a modest correlation with NAO compared to the strong correlation with negative EA  
78 (Skirris et al., 2012; Papadopoulos et al., 2012). Ultimately, while weak westerlies during  
79 negative NAO result in cold temperature in Europe, the most severe winters occur during  
80 negative EA due to the deflection of the maritime westerly flow to the North around the  
81 anticyclonic cell returning as cold and dry northerly continental winds over Europe and the  
82 Northwestern Mediterranean Sea (Fig. 1) (Häkkinen et al., 2011). Yet, interactions exist  
83 between the two modes (Moore and Renfrew, 2011). Indeed, bivariate reconstructions have

84 shown that EA modulates the strength and position of NAO centers of action and that winter  
85 severity is enhanced when both modes are in negative phase. This would for instance explain  
86 that despite similar negative NAO values, winter in Europe was much cooler in 2010  
87 (negative EA) than in 2009 (positive EA) (Moore and Renfrew, 2011).

88 Mistral exerts a strong control on the SSTs in the Northwestern Mediterranean Sea and is  
89 responsible for among the coldest values found in the Gulf of Lions (GoL). Mistral also  
90 triggers intense blooms in February, March and April (FMA) when it is stronger (Bosc et al.,  
91 2004; Durrieu de Madron et al., 2013). A relationship between primary production maxima,  
92 Mistral and negative EA has also been evidenced by Olita et al. (2011). Because Mistral  
93 concurrently causes surface cooling and high primary production, alkenone-derived SSTs in  
94 the GoL are expected to well capture past changes of atmospheric conditions promoting  
95 Mistral. These unique properties motivated the choice of GoL shelf sediment for generating a  
96 high-resolution SST reconstruction over the Common Era using alkenone as a temperature  
97 proxy. Based on this time series we investigate the links between mid-latitude atmospheric  
98 variability, Mistral and SSTs in the GoL with a focus on the strong amplitude SST  
99 fluctuations observed during the Little Ice Age (LIA).

100

## 101 **2. Material and methods**

### 102 **2.1 Analytical procedure**

103 A gravity core KSGC-31 (GMO2-Carnac cruise in 2002, R/V “Le Suroît”) and multi-core  
104 Gol-Ho1B (GolHo cruise in 2013, R/V “Néréis”) were retrieved at virtually the same location  
105 (43°0’23N; 3°17’56E, water depth 60 m, Fig. 1) in the Rhone river mud belt deposited onto  
106 the GoL continental mid-shelf.

107 The two sediment cores were sampled continuously at a sampling step of 1 cm and freeze-  
108 dried overnight. Between 2 - 3 g of dried sediments were extracted with a mixture of  
109 methanol/methylene chloride (1:2 v/v) to recover the lipid biomarkers. Alkenones were

110 further isolated from the total lipid extract by silica gel chromatography using solvent  
111 mixtures of increasing polarity. Gas chromatography (GC) analyses were performed on a  
112 Varian CX 3400 gas chromatograph equipped with a fused CP-Sil-5 silica capillary column  
113 (50 m x 0.32 mm i.d.) and a flame ionization detector. Helium was used as carrier gas. The  
114 oven was temperature programmed from 100°C to 300°C at a rate of 20°C min<sup>-1</sup>. 5 $\alpha$ -  
115 cholestane was added prior GC analyses for quantitation. Details on the analytical procedure  
116 can be found in Ternois et al. (1996).

117 Alkenones are primarily biosynthesized by the ubiquitous haptophyte algae *Emiliana huxleyi*.  
118 This compound series comprises a suite of methyl and ethyl C<sub>37</sub> to C<sub>39</sub> ketones with two or  
119 three double bonds. The C<sub>37</sub> alkenones are used to calculate the C<sub>37</sub> unsaturation index U<sub>37</sub><sup>K</sup> (U<sub>37</sub><sup>K</sup>  
120 = C<sub>37:2</sub>/(C<sub>37:2</sub>+C<sub>37:3</sub>)) now a well-established temperature proxy in paleoceanographic studies.  
121 SSTs were calculated from the downcore U<sub>37</sub><sup>K</sup> values and the most recent global calibration  
122 published by Conte et al. (2006) ( $T = -0.957 + 54.293(U_{37}^K) - 52.894(U_{37}^K)^2 + 28.321(U_{37}^K)^3$ ,  
123 standard error estimate: 1.2°C). Precision based on triplicate alkenone analyses is 0.01 U<sub>37</sub><sup>K</sup>  
124 unit, which in the temperature range considered here, translates into 0.3°C.

125

## 126 **2.2 Chronology**

127 Age control for the multi-core Gol-Ho1B is based on <sup>210</sup>Pb dating and for gravity core  
128 KSGC31 on both <sup>210</sup>Pb and <sup>14</sup>C dating. For the gravity core, 10 radiocarbon dates were  
129 acquired on bivalve shells with the ARTEMIS accelerator mass spectrometer (AMS) operated  
130 in the Laboratoire de Mesure du Carbone 14, Saclay (France). Radiocarbon ages were  
131 corrected for local reservoir effect of  $\Delta R = 23 \pm 71$  (Table 1) and converted into 1 $\sigma$  calendar  
132 years using the CALIB7.1 software and the marine calibration curve Marine13 (Stuiver and  
133 Reimer, 1993; Reimer et al., 2013). Linear interpolation was performed between <sup>14</sup>C-dated  
134 horizons to translate each sampling depth to age expressed here in Anno Domini (AD) years  
135 (Fig. 2). Because the two upper most <sup>14</sup>C dates indicate post-bomb ages (calibrated using

136 OxCal 4.2; Ramsey and Lee, 2013) additional  $^{210}\text{Pb}$  and  $^{137}\text{Cs}$  measurements were performed  
137 in the first 10 cm of the gravity core KSGC31 (Table 2). Note that the  $^{14}\text{C}$  date at 18.5 cm  
138 ( $1570 \pm 78$  yr AD) was considered as an outlier and discarded from the age model as it  
139 appeared incompatible with the  $^{14}\text{C}$  modern age of the above horizons (5.5 and 11.5 cm) and  
140 the presence of  $^{210}\text{Pb}$  and  $^{137}\text{Cs}$  in the upper 10 cm.

141 Activities of  $^{210}\text{Pb}$ ,  $^{226}\text{Ra}$ ,  $^{137}\text{Cs}$  and  $^{232}\text{Th}$  were determined in the gravity core KSGC-31 and  
142 multi-core Gol-Ho1B by  $\gamma$  spectrometry using a low-background high-efficiency well-shaped  
143 germanium detector equipped of a Cryo-cycle (CANBERRA; Schmidt et al., 2014) (Fig. 3).  
144 The calibration of the detector was achieved using certified IAEA reference materials (RGU-  
145 1; RGTh; IAEA-135). Activities are expressed in  $\text{mBq g}^{-1}$  and errors based on  $1\sigma$  counting  
146 statistics.  $^{210}\text{Pb}$  excess ( $^{210}\text{Pb}_{\text{xs}}$ ) was determined by subtracting the activity supported by its  
147 parent isotope  $^{226}\text{Ra}$  from the total  $^{210}\text{Pb}$  activity in the sediment. Errors in  $^{210}\text{Pb}_{\text{xs}}$  were  
148 calculated by propagation of errors in the corresponding pair ( $^{226}\text{Pa}$  and  $^{210}\text{Pb}$ ). To compensate  
149 for potential effect of compositional changes of sediments and to optimize splicing of the  
150 multicore and gravity core records,  $^{210}\text{Pb}_{\text{xs}}$  activities were normalized using  $^{232}\text{Th}$   
151 concentrations measured simultaneously by  $\gamma$ counting ( $^{210}\text{Pb}_{\text{xs}}^{\text{Th}}$ ).

152 Depth profiles of  $^{232}\text{Th}$ ,  $^{210}\text{Pb}_{\text{xs}}^{\text{Th}}$  and  $^{137}\text{Cs}$  activities for multicore Gol-Ho1B were determined  
153 shortly after collection at sea and prior biomarker analyses.  $^{210}\text{Pb}_{\text{xs}}^{\text{Th}}$  values show a mixed  
154 layer in the upper 4 cm, followed by an exponential decrease with increasing depth in the core  
155 (Table 2, Fig. 3B) from which sediment age is calculated. Sediment accumulation rates were  
156 derived from the  $^{210}\text{Pb}_{\text{xs}}^{\text{Th}}$  profile assuming constant flux and constant sedimentation  
157 accumulation rates (referred to as the CF:CS model, Schmidt et al. 2014). To account for  
158 compaction effect,  $^{210}\text{Pb}_{\text{xs}}^{\text{Th}}$  values were plotted against cumulative mass. A mean Mass  
159 Accumulation Rate (MAR) of  $0.31 \text{ g cm}^{-2} \text{ yr}^{-1}$  was estimated. The deposition time (in years)  
160 of each sediment layer was obtained by dividing the cumulated dry mass per unit area by the  
161 MAR (Fig. 3D). The deposition year was subsequently estimated based on the sampling year  
162 of the core, in 2013. The  $^{210}\text{Pb}$  chronology indicates that the multicore Gol-Ho1B ranges from

163 1960 ( $\pm 5.6$ ) to 2013 AD.  $^{137}\text{Cs}$  was detected throughout the multi-core in agreement with the  
164 well-known pulse inputs related to the nuclear weapon test fall-out in the early sixties  
165 (maximum atmospheric fallout is in 1963 in the Northern Hemisphere) (Fig. 3C, Table 2).  
166 Comparison between  $^{232}\text{Th}$ ,  $^{210}\text{Pb}_{\text{xs}}$  and  $^{137}\text{Cs}$  activities in KSGC31 and Gol-Ho1B cores was  
167 used to determine the material loss during gravity coring and to splice records. A shift in  
168 depth of 15 cm gave the best correspondence between the two profiles (Fig. 3) leading to a  
169 core-top age of 1971 ( $\pm 1.4$ ) AD for the gravity core KSGC31.

170 For the multicore Gol-Ho1B sediment, the sedimentation rate decreases from  $0.47 \text{ cm yr}^{-1}$  at  
171 the water-sediment interface to  $0.32 \text{ cm yr}^{-1}$  at the base of the core. In the gravity core  
172 KSGC31, sedimentation rate determined for the upper 10 cm is estimated to be around  $0.16$   
173  $\text{cm yr}^{-1}$  (without porosity values for the gravity core MAR could not be calculated).  
174 Sedimentation rate for the underlying layers derived from  $^{14}\text{C}$  dating is on the order of  $0.1 \text{ cm}$   
175  $\text{yr}^{-1}$ . Lower sedimentation rates in the gravity core compared to the multicore is not unusual  
176 and explained by increasing natural compaction of sediment with depth and possibly also by  
177 compaction due to the gravity coring (Sicre et al., 2011).

178

### 179 **3. Results**

#### 180 **3.1. Industrial Era period**

181 Fig. 4A shows the SST reconstruction since 1850 AD obtained for the upper gravity core  
182 KSGC31 (dark green solid line) and entire multicore Gol-Ho1B (light green dashed line)  
183 records against age, based on the  $^{210}\text{Pb}$  and  $^{14}\text{C}$  chronology. Values range from  $16.5$  to  $18^\circ\text{C}$   
184 in the gravity core, and from  $16.5$  to  $19^\circ\text{C}$  in the multicore. Both records indicate comparable  
185 SST values in the overlapping interval except for the warmest value in the mid-1960s ( $\sim$   
186  $19^\circ\text{C}$ ) seen in multi-core sediment but not in the gravity core sediment. We interpreted this  
187 result by a probable artifact in the uppermost cms of the gravity core due to coring as  
188 suggested by smoothing in the exponential decay in the  $^{210}\text{Pb}$  curve (Fig. 3B). Indeed, gravity

189 coring generally causes material loss and the disturbance of the uppermost sediment layers  
190 while a multi-corer typically recovers intact surface sediment. The two-fold difference in  
191 sedimentation rates (0.32 versus 0.16 cm yr<sup>-1</sup>) between the two records in this interval  
192 translates into a difference of temporal resolution that could also account for this discrepancy.  
193 In any case, all values were considered to construct the spliced record (Fig. 4B, Fig. 5A). The  
194 full 2k SST reconstruction was thus obtained by combining the gravity core KSGC31 SST  
195 values from 0 to 1971 AD and the complete multicore Gol-Ho1B SST data spanning from  
196 1960 to 2013 AD. As can be seen in Figure 4B, the SST signal depicts an overall warming  
197 ranging from ~16.5°C to ~19°C during the 20<sup>th</sup> century followed by cooling over the most  
198 recent decades. Multi-decadal scale fluctuations are superimposed to this trend. These values  
199 are among the lowest of the Mediterranean surface waters in agreement with the temperature  
200 field of the Mediterranean Sea shown in Figure 1 and previous alkenone SST data obtained  
201 from surface sediments distributed across the NW Mediterranean Sea pointing to colder SSTs  
202 in the GoL (Ternois et al., 1996).

### 203 **3.2. The Common Era (last 2k)**

204 Figure 6A plots the full past 2k SST record of the GoL. A 25-yr binning was applied (black  
205 line) in order to easily evaluate departures from the average value (16.7°C ± 0.7°C). The first  
206 millennium AD reveals several cold excursions of ~ 1.5°C and a mean value cooler by 1.7°C  
207 than the 20th century mean (17.9°C). During the MCA (ca. 1000 - 1200 AD) SSTs were  
208 warmer (~ 16.9°C) but ~ 1°C lower than the 20th century. Around 1200 AD, they  
209 progressively decline and display marked multi-decadal fluctuations with well-expressed  
210 minima (ca. ~ 16°C) around 1300 AD, 1500 AD, mid-16s AD and mid-17s AD, each  
211 followed by warm spells, the most outstanding by duration and amplitude (~ 2°C in few  
212 decades) centered at ~ 1700 AD. As a result, average SSTs for the LIA (1400 - 1850 AD)  
213 were 1.3°C colder than the 20th century and not as cold as the first millennium during which  
214 post-cooling temperature rebounds above average are absent. In the following section, we

215 compare the proxy and instrumental data and analyze the full 2k SST reconstruction with a  
216 focus on the high amplitude SST oscillations of the LIA.

## 217 **4. Discussion**

### 218 **4.1. The Industrial Era SST signal**

219 Figures 5 shows the Gol-Ho1B\_KSGC-31 spliced SST reconstruction, the instrumental  
220 annual mean and late winter-early spring (FMA) temperature time series average over a 5°x  
221 5° grid from Kaplan SST V2 data  
222 ([http://www.esrl.noaa.gov/psd/data/gridded/data.kaplan\\_sst.html](http://www.esrl.noaa.gov/psd/data/gridded/data.kaplan_sst.html)) since the late 19<sup>th</sup> century.

223 Both proxy and instrumental data show a long-term warming trend over the 20th century. The  
224 alkenone SSTs rise since 1900 AD is ~1.7°C but reaches ~2.2°C when considering the 20th  
225 century only, i.e. after removing the last cold decade (2000-2012). These estimates are close  
226 to the value of 0.026 °C yr<sup>-1</sup> obtained from satellite SSTs for the W Mediterranean Sea over  
227 the 1985 - 2008 period, and 0.022°C yr<sup>-1</sup> of the NOCS *in situ* SSTs from 1973 to 2008 (Skiriris  
228 et al., 2012). Alkenone SSTs indicate values closer to the annual mean than FMA (Fig. 5)  
229 suggesting that alkenone production does not only take place during the months of intense  
230 Mistral (Bosc et al., 2004; Durrieu de Madron et al., 2013) but also during the warm season  
231 (late spring to summer). Vertical mixing induced by Mistral would thus sustain primary  
232 production over a longer season by replenishing surface waters with nutrients.

233 The SSTs decline since the beginning of the 21th century can be related to several severe  
234 winters such as the coldest on record in Europe and United Kingdom, in 2010/2011 that  
235 Moore and Renfrew (2011) attributed to combined negative NAO and EA states. These  
236 authors showed that EA<sup>-</sup> NAO<sup>-</sup> accounted for 50% of the winter temperature that year against  
237 20% by NAO alone, outlining the value of considering both modes to better describe climate  
238 conditions. Winter 2012 was another exceptionally cold winter associated with a strong  
239 anticyclonic blocking in the NA (Durrieu de Madron et al., 2013) that could account together  
240 with winter 2010/2011 for the cold uppermost SST value. During the 20<sup>th</sup> century, cold SSTs  
241 in the 70s to early 80s are also noteworthy both in the proxy and instrumental data (Fig. 5A,

242 5B, 5C). They coincide with a period of strongly negative EA (Fig. 5D) and episodes of major  
243 dense water formation in the GoL (Béthoux et al., 2002) in accordance with the role of EA on  
244 SSTs in the GoL. Regression between EA index and SSTs on 5 yr binned values since 1950  
245 were calculated to account for age model uncertainties. The obtained Pearson correlation  
246 coefficient,  $r = 0.45$  (at the 95% confidence interval) is close to values calculated using  
247 instrumental data (0.58 for NOCS in situ SSTs and 0.50 for satellite SSTs in the W  
248 Mediterranean, at the 95% confidence interval) (Skirris et al., 2012).

#### 249 **4.2. General SST trends over the past 2000 yr**

250 In this section, we compare the SST signal of the GoL with other Mediterranean and North  
251 Atlantic records that may have features in common (Fig. 6). Records that document centennial  
252 scale SST variability in the Mediterranean during the Common Era are very scarce. They  
253 belong to different sectors of the W-Mediterranean basin, i.e. the Alboran Sea (Fig. 6B ~ 30  
254 yr time resolution; Nieto-Moreno et al., 2013) and Balearic basin (Fig. 6C; ~ 30 yr time  
255 resolution; Moreno et al., 2012) and cover all or part of the CE. None of them have a  
256 chronostratigraphic control during the instrumental period to evaluate the relationship  
257 between SSTs and climate processes. The high-resolution SST reconstruction from North  
258 Iceland (MD99-2275; Sicre et al., 2008) was also considered for a regional analysis of the  
259 data because its cross-analysis with instrumental data has shown a strong control of NAO on  
260 SSTs (Sicre et al., 2011). Precision on the age model of this core based on tephrochronology  
261 is on the order of the decade while for the other cores it is on the order of several decades  
262 (Table 1).

263 All records shown in Fig. 6 are based on alkenone SSTs, but primary production patterns have  
264 different characteristics depending on the location of each core in the Mediterranean Sea.  
265 While the GoL belongs to a blooming regime tightly linked to Mistral, the Alboran and  
266 Balearic Sea relate to different primary production patterns as defined by D'Ortenzio and  
267 Ribera d'Alcala (2009). In the Balearic Sea, chlorophyll concentrations show algal blooms of  
268 moderate amplitude and variable timing that occur in spring sporadically. This area thus

269 combines periods of enhanced production with oligotrophic conditions leading to an erratic  
270 regime classified as an intermittently blooming region (D'Ortenzio and Ribera d'Alcala,  
271 2009). In the Alboran Sea, the seasonal cycle of phytoplankton production is the most chaotic  
272 of the Mediterranean (D'Ortenzio and Ribera d'Alcala, 2009). Primary production exhibits a  
273 strong inter-annual variability with a pronounced production peak in February - March and in  
274 fall (October). It is also strongly influenced by Atlantic inflow waters and meso-scale gyre  
275 induced upwelling which all together leads to confounding response of phytoplankton to  
276 physical forcings (Bosc et al., 2004; D'Ortenzio and Ribera d'Alcala, 2009). These cores thus  
277 belong to biogeographical clusters with temporal and dynamical regimes that are distinct from  
278 the GoL, including in its unique link to atmospheric forcing (see Fig. 4 in D'Ortenzio and  
279 Ribera d'Alcala, 2009). Considering age model uncertainties, lower temporal resolution and  
280 the lack of instrumental control to evaluate the ability of local alkenone SSTs to capture  
281 climatic information, only broad features of the records were examined for this comparison.

282 As can be seen in Fig. 6, the long-term cooling ending at ~ 1800 AD is shared by all almost  
283 sites and consistent with the recent finding of McGregor et al. (2015) of a global ocean  
284 cooling from 0 to 1800 AD that, according to model simulations of the pre-industrial  
285 millennium climate (801 – 1800 AD) would be imputable to volcanism. This trend reversed in  
286 the GoL and Alboran Sea around 1800 AD, but persisted off N. Iceland because of sustained  
287 sea ice occurrence, even in lower abundance during 20th century than the LIA (Marcias-  
288 Fauria et al., 2010). Unexpectedly, the absence of warming is also notable in the Balearic  
289 record as modern SSTs show rising values both in the Eastern and Western Mediterranean  
290 (Skirris et al. 2012; Papadopoulos et al., 2012) and in European land-based T reconstructions  
291 (Luterbacher et al., 2004). The lack of age control of the past ca. 500 yr (Fig. 6C, dashed  
292 lines) and extrapolation of the age model in the upper core is the probable explanation for this  
293 discrepancy. Another salient feature of these SST records, in common with the GoL, is the  
294 distinctly cooler first millennium as compared to the MCA off N. Iceland while in the  
295 Balearic basin it is almost muted. In contrast, the last millennium cooling at the onset of the

296 LIA is observed in all records, though not synchronously. It is much abrupt off N. Iceland due  
297 to the imprint of sea ice on SSTs associated with the southward shift of the polar front under  
298 weakened NAO (Trouet et al., 2009).

299 As earlier outlined, the most outstanding feature of the GoL SST signal is the high amplitude  
300 oscillations and in particular the rebounds above the mean observed during the LIA that are  
301 not seen during the first millennium. Interestingly, while sea ice was common in the North  
302 Atlantic (Massé et al., 2008) and the northward oceanic heat transport reduced (Lund et al.,  
303 2006) during the LIA, the first millennium is a period of minimum sea ice cover and  
304 enhanced northward advection of heat. In the next section we investigate causes for the  
305 outstanding SST fluctuations of the LIA in the GoL and explore past changes in atmospheric  
306 modes of variability and notably EA.

#### 307 **4.3 SSTs and large-scale climate variability modes over the last millennium**

308 Multidecadal to centennial scale variability of the GoL SSTs over the past 1000 yr (Fig. 7E) is  
309 explored in light of high-resolution proxy data from the adjacent North Atlantic, i.e. Iceland  
310 (Sicre et al., 2011; Larsen et al., 2013; Ólafsdóttir et al., 2013; Fig. 7B, 7C), the Iceland Basin  
311 (Moffa-Sanchez et al., 2014, Fig. 7D), the Swiss Alp glaciers (Holzhauser et al., 2005, Fig.  
312 7A), and western Europe land temperatures (Luterbacher et al., 2004, Fig. 7F), as well as the  
313 NAO index (Ortega et al., 2015; Fig. 7G) and solar activity reconstructed by Steinhilber et al.  
314 (2012) (Fig. 7H) to investigate the role of large-scale atmospheric low frequency variability  
315 and oceanic processes.

316 Previous proxy reconstructions have shown that during the MCA surface waters were  
317 generally warmer along the path of the North Atlantic Current (Keigwin, 1996; Sicre et al.,  
318 2008; Richter et al. 2009) due to stronger Atlantic Meridional Overturning Circulation  
319 (AMOC) consistent with the hypothesis that positive NAO phase (Fig. 7H) prevailed during  
320 this period and that strong NAO enhances AMOC (Delworth and Greatbach, 2000).  
321 Relatively warm and/or wet summers resulted in increase melting and glacier retreat in  
322 Iceland (Larsen et al., 2013; Ólafsdóttir et al., 2013) (Fig. 7B) and in the Alps (Holzhauser et

323 al., 2005; Denton and Broecker, 2008) (Fig. 7A). Off North Iceland, the stepwise SST  
324 increase ~ 1000 AD indicates a northward migration of the polar front within a few decades  
325 (Fig. 7C) a feature that is not seen in the Mg/Ca of *G. inflata* South of Iceland (RAPiD17-15,  
326 6yr time resolution; Fig. 7D) where surface water properties are mainly shaped by the  
327 strength of the subpolar gyre (Moffa-Sanchez et al., 2014). In the GoL, SSTs also generally  
328 warm (Fig. 7E). The transition to colder conditions between 1200 and 1300 AD, depending  
329 on the records, is thought to be related to a weakening of NAO leading to colder climate in  
330 the North Atlantic and the adjacent Euro-Mediterranean region (Trouet et al., 2009).

331 All independent proxy records shown in Fig. 7 point to more severe conditions during the LIA  
332 and the return of seasonal sea ice but with differences in the decadal structure of the signals.  
333 SSTs in the GoL and S. Iceland basin (Fig. 7D, 7E) indicates that cooling occurred in parallel  
334 during the early LIA (1400 to 1550 AD), but tend to vary in opposite phase during the Late  
335 LIA. Notably, between 1530 and 1680 AD, cold SSTs in the GoL contrast with warm surface  
336 waters South of Iceland confirming previous findings of Richter et al. (2009) at Feni drift of  
337 unexpected mild conditions in the subpolar North Atlantic. According to Larsen et al. (2013)  
338 this warmth would have been responsible for the retreat of the Langjökull ice cap from 1550  
339 to 1680 AD (Fig. 7B). Advection of temperature anomalies from the tropical Atlantic  
340 combined with reduced heat loss to the atmosphere under weakened NAO have been  
341 proposed as possible explanations for these unexpected warm conditions during the LIA  
342 under reduced AMOC (Richter et al., 2009). Concomitantly, coldest winters in Europe  
343 supported by the multiproxy reconstruction of Luterbacher et al. (2004) ((Fig. 7F) and the  
344 expansion of Swiss glacier (Fig. 7A; Holzhauser et al., 2005; Denton and Broecker, 2008)  
345 evidence a W-E temperature asymmetry between the cold Euro-Mediterranean climate and  
346 warm subpolar waters during this time interval. This spatial pattern contrasting warm  
347 subpolar surface waters upstream the NA anticyclonic cell with cold temperatures in  
348 downstream regions (Europe and Mediterranean Sea) is expected from blocked regimes  
349 during negative EA (Häkkinen et al., 2011). Co-eval enhanced sea ice and lower SSTs in the

350 Nordic Seas (off N. Iceland) is also coherent with EA driven spatial SST pattern today  
351 (Cassou et al., 2011). Severe conditions during the LIA in the Euro-Mediterranean region can  
352 thus be seen as resulting from enhanced frequency of blocking regimes associated with  
353 negative EA on longer time scale (Cassou et al., 2011). This hypothesis is supported by  
354 modeling experiments performed for the second half of the 20<sup>th</sup> century and the Late Maunder  
355 Minimum (1645 – 1715 AD) showing that NA blocking is favored by lower solar activity that  
356 prevailed during the LIA (Nesmé-Ribes et al., 1993; Barriopedro et al., 2008). Rebounds  
357 above average would in turn reflect rapid shifts of the EA state towards more positive values  
358 implying stronger links with the subtropical climate and weaker Mistral. Overall, this set of  
359 proxy records exhibits a spatial temperature pattern that is coherent in sign with persistent  
360 anticyclone blocking and negative EA promoted by low solar activity of the LIA (Fig. 7H), in  
361 particular towards the Late LIA. Our interpretation of the GoL data together with high-  
362 resolution records distributed across the NA/Euro-Mediterranean region thus supports the  
363 hypothesis that EA played an important role in the (late) LIA climate early formulated based  
364 on one single record in the NA (RAPiD17-15) by Moffa-Sanchez et al. (2014).

## 365 **5. Conclusions**

366 A unique SST reconstruction resolving decadal variability was developed over the full  
367 Common Era from shelf sediments in the convection region of the GoL (NW Mediterranean  
368 Sea). The tight link between alkenone-derived SSTs, Mistral and EA, the dominant mode of  
369 variability in the Mediterranean Sea, was used to investigate the climate of the Common Era  
370 in the NW-Mediterranean Sea and notably the strong fluctuations of the LIA. Comparison  
371 between instrumental and proxy data over the 20th century revealed a similar warming trend  
372 of about 2°C. SSTs during the MCA (1000 – 1200 AD) were among the warmest of the pre-  
373 industrial last millennium though ~ 1°C lower than those of the 20<sup>th</sup> century. Most of the first  
374 millennium (200 -800 AD) and the LIA both indicate cold climate conditions but the LIA  
375 differ by the presence of remarkable cold extremes followed by above average temperature  
376 rebounds. Cold decades were found to reflect strong heat loss caused by negative EA and

377 associated NA blocking regimes creating the conditions for intensified and cold Mistral flow.  
378 Regional synthesis of high-resolution land and marine time series from the NA and Euro-  
379 Mediterranean region further highlighted a W-E temperature asymmetry during the late LIA  
380 that is spatially coherent with persistent blocked regimes under negative EA and weak NAO.  
381 Reinforced northerly flow (Mistral) over Western Europe would have been favored by low  
382 solar activity.

383 **ACKNOWLEDGMENTS:** We thank CNRS and the MISTRALS/PALEOMEX program for  
384 financial support and the Ocean2k working group of the Past Global Changes (PAGES)  
385 project for discussions. We are very grateful to Nabil Sultan, Ifremer for providing facilities at  
386 sea and the crew operating the GMO2 Carnac cruise. We are also thankful for the crew of the  
387 N/V Néréis of the “Observatoire Océanographique de Banuyls” (OOB). We also thank the  
388 Laboratoire de Mesure du Carbone 14, UMS 2572, ARTEMIS for 14C measurements by  
389 mass accelerator spectrometry in the frame of the National Service to CNRS, CEA, IRD,  
390 IRSN and Ministère de la Culture et de la Communication. B.M. wishes to express her thanks  
391 to the CSIC-Ramón y Cajal post-doctoral program RYC-2013-14073 and the Shackleton  
392 Fellowship (Clare Hall College). This dataset is available on the NOAA database  
393 (<http://www.esrl.noaa.gov/>).

394

- 396 Alpert, P., Baldi, M., Ilani, R., Krichak, S., Price, C., Rodo, X., Saaroni, H., Ziv, B., Pavel Kishcha, P.,  
397 Barkan, J., Mariotti, A., and Xoplaki, E., 2006. Relations between climate variability in the  
398 Mediterranean region and the tropics: ENSO, South Asian and African monsoons, hurricanes and  
399 Saharan dust. *Developments in Earth and Environmental Sciences*, 4, 149-177.
- 400 Barriopedro, D., García-Herrera, R., Huth, R., 2008. Solar modulation of Northern Hemisphere winter  
401 blocking. *J. Geophys. Res. Atmos*, 113, D14118.
- 402 Béthoux, J.P., Durieu de Madron, X., Nyffeler, F., Tailliez, D., 2002, Deep water in the western  
403 Mediterranean: peculiar 1999 and 2000 characteristics, shelf formation hypothesis, variability since  
404 1970 and geochemical inferences. *J. Mar. Sys.*, 33-34, 117-131.
- 405 Bosc, E., Bricaud, A., Antoine, D., 2004. Seasonal and interannual variability in algal biomass and  
406 primary production in the Mediterranean Sea, as derived from 4 years of SeaWiFS observations.  
407 *Glob. Biogeochem. Cycles*, 18, 1-17.
- 408 Burlando, M., 2009. The synoptic-scale surface wind climate regimes of the Mediterranean Sea  
409 according to the cluster analysis of ERA-40 wind fields, *Theor Appl. Climatol.*, 96, 69-83.
- 410 Cassou, C., Minvielle, M., Terray, L., Perigaud, C., 2011. A statistical-dynamical scheme for  
411 reconstructing ocean forcing in the Atlantic. Part I: weather regimes as predictors for ocean surface  
412 variables. *Climate Dynamics*, 36, 19-39.
- 413 Conte, M.H., Sicre, M.-A., Rühlemann, C., Weber, J.C., Schulte, S., Schulz-Bull, D., Blanz, T., 2006.  
414 Global temperature calibration of the alkenone unsaturation index (UK37) in surface waters and  
415 comparison with surface sediments. *Geochem. Geophys. Geosyst.*, 7, Q02005.
- 416 Delworth T.L., Greatbach, R., 2000. Multidecadal thermohaline circulation variability driven by  
417 atmospheric surface flux forcing. *J. of Clim.*, 13, 1481-1495.
- 418 Denton, G.H., Broecker, W.S., 2008. Wobbly ocean conveyor circulation during the Holocene? *Quat.*  
419 *Sci. Rev.* 27, 1939-1950
- 420 Durrieu de Madron, X., Houpert, L., Puig, P., Sanchez-Vidal, A., Testor, P., Bosse, A., Estournel, C.,  
421 Somot, S., Bourrin, F., Bouin, M. N., Beauverger, M., Beguery, L., Calafat, A., Canals, M., Cassou,  
422 C., Coppola, L., Dausse, D., D'Ortenzio, F., Font, J., Heussner, S., Kunesch, S., Lefevre, D., Le  
423 Goff, H., Martín, J., Mortier, L., Palanques, A., Raimbault, P., 2013. Interaction of dense shelf water

424 cascading and open-sea convection in the northwestern Mediterranean during winter 2012. *Geophys.*  
425 *Res. Lett.* 40, 1379-1385.

426 D'Ortenzio, F., Ribera d'Alcala M., 2009. On the trophic regimes of the Mediterranean Sea: a satellite  
427 analysis. *Biogeosciences*, 6, 1-10.

428 Häkkinen, S., Rhines, P.B., Worthen, D.L., 2011. Atmospheric blocking and Atlantic multidecadal  
429 ocean variability. *Science*, v. 334, no. 6056, p. 655-659.

430 Holzhauser, H., Magny, M., Zumbühl, H.J., 2005. Glacier and lake-level variation in west-central  
431 Europe over the last 3500 years. *The Holocene* 15, 789–801.

432 Hurrell, J.W., 1995. Decadal trends in the North Atlantic Oscillation: regional temperatures and  
433 precipitation. *Science* 269, 676-679.

434 Jiang, Q., Smith, R.B., Doyle, J. 2003. The nature of the mistral: Observations and modelling of two  
435 MAP events. *Q.J.R. Meteorol. Soc.* 129, 857-875. doi:10.1256/qj.02.21

436 Josey, S.A., Somot, S., Tsimplis, M., 2011, Impacts of atmospheric modes of variability on  
437 Mediterranean Sea surface heat exchange. *Journal of Geophysical Research: Oceans*, v. 116, p.  
438 C02032.

439 Kaplan, A., Cane, M., Kushnir, Y. Clement, A., Blumenthal, M., Rajagopalan, B., 1998. Analyses of  
440 global sea surface temperature 1856-1991. *Journal of Geophysical Research*, 103, 18,567-18,589

441 Keigwin, L.D., 1996. The little ice age and medieval warm period in the Sargasso Sea. *Science*, 274,  
442 1504-1508.

443 Knight, J.R., Folland, C.K., Scaife, A.A., 2006. Climate impacts of the Atlantic Multidecadal  
444 Oscillation. *Geophys. Res. Lett.*, 33, L17706, doi:1029/2006GL026242.

445 Larsen, D.J., Miller, G.H., Geirsdóttir, Á., 2013. Asynchronous Little Ice Age glacier fluctuations in  
446 Iceland and European Alps linked to shifts in subpolar North Atlantic circulation. *Earth and Planet.*  
447 *Sci. Lett.* 380, 52-59.

448 Lionello, P., Malanotte-Rizzoli, P., Boscolo, R., Alpert, P., Artale, V., Li, L., Luterbacher, J., May, W.,  
449 Trigo, R., Tsimplis, M., Ulbrich, U., Xoplaki, E., 2006. The Mediterranean climate: An overview of  
450 the main characteristics and issues, *in* Lionello P. and Boscolo, R., eds. *Developments in Earth and*  
451 *Environmental Sciences*, Volume 4, Elsevier, p. 1-26.

452 Lund, D.C., Lynch-Steiglitz, J., Curry, W.B., 2006. Gulf Stream density structure and transport during  
453 the past millennium. *Nature*, 444, doi:10.1038/nature05277.

454 Luterbacher, J., Dietrich, D., Xoplaki, E., Grosjean, M., Wanner, H., 2004. European seasonal and  
455 annual temperature, trends and extremes since 1500. *Science*, 303, 1499-1503.

456 Massé, G., Rowland, S.J., Sicre, M.-A., Jacob, J., Jansen, E., Belt, S.T., 2008. Abrupt climate changes  
457 for Iceland during the last millennium: Evidence from high-resolution sea ice reconstructions. *Earth  
458 and Planet. Sci. Lett.* 269, 565-569.

459 Marcias-Fauria, M., Grinsted, A. Helama, S. Moore, J. Timonen, M. Martma, T. Isaksson, E. Eronen,  
460 M., 2010. Unprecedented low twentieth century winter sea ice extent in the Mestern Nordic Seas  
461 since A.D. 1200. *Clim. Dyn.* 34, 781-795.

462 Mariotti, A., Dell'Aquila, A., 2012. Decadal variability in the Mediterranean region: role of large scale  
463 forcing and regional processes. *Clim. Dyn.* 38, 1129-1145.

464 Marullo, S., Artale, V., Santoleri, R., 2011. The SST multidecadal variability in the Atlantic-  
465 Mediterranean region and its relation to AMO. *J. of Clim.*, 4385- 4401.

466 Moffa-Sanchez, P., Born, A., Hall, I.R., Thornalley, D.J.R., Barker, S., 2014. Solar forcing of North  
467 Atlantic surface temperature and salinity over the past millennium. *Nature Geosci*, 7, 275-278.

468 McGregor, H.V., Evans, M.N., Goose, H., Leduc, G., Martrat, B., Addison, J.A., Mortyn, P.G., Oppo,  
469 D.W., Seidenkrantz, M.-S., Sicre, M.-A., Phipps, S.J., Selvaraj, K., Thirumalai, K. , Filipsson, H.,  
470 Ersek, V., 2015. Robust global ocean cooling trend for the pre-industrial Common Era. *Nat. Geosci.*  
471 doi:10.1038/NGEO2510.

472 Moore, G.W.K., Renfrew, I.A., 2011. Cold European winters: interplay between the NAO and the East  
473 Atlantic mode. *Atmos. Sci. Lett.* 13, 1-8.

474 Moreno, A., Pérez, A., Frigola, J., Nieto-Moreno, V., Rodrigo-Gámiz, M., Martrat, B., González-  
475 Sampériz, P., Morellón, M., Martín-Puertas, C., Corella, J.P., Belmonte, Á., Sancho, C., Cacho, I.,  
476 Herrera, G., Canals, M., Grimalt, J.O., Jiménez-Espejo, F., Martínez-Ruiz, F., Vegas-Vilarrúbia, T.,  
477 Valero-Garcés, B.L., 2012. The Medieval Climate Anomaly in the Iberian Peninsula reconstructed  
478 from marine and lake records. *Quat. Sci. Rev.*, 43, 16-32.

479 Najac, J., Boè, J., Terray L., 2009. A multi-model ensemble approach for assessment of climate change  
480 impact on surface winds in France. *Clim. Dyn.* 32, 615-634.

481 Nesmé-Ribes, E., Ferreira E.N., Sadourny R., Le Treut H. Li, Z.L., 1993. Solar dynamics and its  
482 impact on solar irradiance and the terrestrial climate. *J. Geophys. Res.* 98, 18923-18935.

483 Nieto-Moreno, V., Martínez-Ruiz, F., Willmott, V., García-Orellana, J., Masqué, P., Sinninghe  
484 Damsté, J.S., 2013. Climate conditions in the westernmost Mediterranean over the last two  
485 millennia: An integrated biomarker approach. *Org. Geochem.* 55, 1-10.

486 Ólafsdóttir, K.B., Geirsdóttir, Á., Miller, G.H., Larsen, D.J., 2013. Evolution of NAO and AMO  
487 strength and cyclicity derived from a 3-ka varve-thickness record from Iceland. *Quat. Sci. Rev.* 69,  
488 142-154.

489 Olita, A., Sorgente, R., Ribotti, A., Fazioli, L., Perilli A., 2011. Pelagic primary production in the  
490 Algero-provençal basin by means of multisensory satellite data: focus on interannual variability and  
491 its drivers. *Ocean Dyn.*, 61, 1005-1016.

492 Ortega, P., Lehner, F., Swingedouw, D., Masson-Delmotte, V., Raible, C.C., Casado, M., Yiou, P.,  
493 2015. A model-tested North Atlantic Oscillation reconstruction for the past millennium. *Nature* 523,  
494 doi:10.1038/nature14518.

495 Papadopoulos, V.-P., Josey, S.-A., Bartzokas, A., Somot, S., Ruiz, S., Drakopoulou, P., 2012. Large-  
496 Scale Atmospheric Circulation Favoring Deep- and Intermediate-Water Formation in the  
497 Mediterranean Sea. *J. Clim.* 25, 6079-6091.

498 Ramsey, C. B., Lee, S., 2013. Recent and planned developments of the program Oxcal. *Radiocarbon*  
499 55, 720-730.

500 Reimer, P. J., Bard, E., Bayliss, A., Beck, J. W., Blackwell, P. G., Bronk Ramsey, C., Buck, C. E.,  
501 Cheng, H., Edwards, R. L., Friedrich, M., Grootes, P. M., Guilderson, T. P., Haflidason, H., Hajdas,  
502 I., Hatté, C., Heaton, T. J., Hoffmann, D. L., Hogg, A. G., Hughen, K. A., Kaiser, K. F., Kromer, B.,  
503 Manning, S. W., Niu, M., Reimer, R. W., Richards, D. A., Scott, E. M., Southon, J. R., Staff, R. A.,  
504 Turney, C. S. M., van der Plicht, J., 2013. IntCal13 and Marine13 Radiocarbon Age Calibration  
505 Curves 0–50,000 Years cal BP. *Radiocarbon*, , 55, 1869–1887, doi: 10.2458/azu\_js\_rc.55.16947.

506 Richter, T.O., Peeters, F.J.C., van Weering, T.C.E., 2009. Late Holocene (0-2.4 ka BP) surface water  
507 temperature and salinity variability, Feni Drift, NE Atlantic Ocean. *Quat. Sci. Rev.* 28, 1941–1955.

508 Schabbar, A., Huang, J., Higuchi, K., 2001. The relationship between the wintertime north Atlantic  
509 Oscillation and blocking episodes in the North Atlantic. *Int. J. of Climatology*, 21, 355-369.

510 Schmidt, S., Howa, H., Diallo, A., Martín, J., Cremer, M., Duros, P., Fontanier, C., Deflandre, B.,  
511 Metzger, E., Mulder, Th., 2014. Recent sediment transport and deposition in the Cap-Ferret Canyon,  
512 South-East margin of Bay of Biscay. *Deep-Sea Res. II* 104, 134-144.

513 Sicre, M.-A., Hall, I.R., Mignot, J., Khodri, M., Ezat, U., Truong, M.X., Eiriksson, J., Knudsen, K.-L.,  
514 2011. Sea surface temperature variability in the subpolar Atlantic over the last two millennia.  
515 *Paleoceanography*, 26, PA4218.

516 Sicre, M.-A., Yiou, P., Eiriksson, J., Ezat, U., Guimbaut, E., Dahhaoui, I., Knudsen, K.-L., Jansen, E.,  
517 Turon, J.-L., 2008. A 4500-year reconstruction of sea surface temperature variability at decadal time  
518 scales off North Iceland. *Quat. Sci. Rev.* 27, 2041-2047.

519 Skliris, N., Sofianos, S., Gkanasos, A., Mantziafou, A., Vervatis, V., Axaopoulos, P., Lascaratos, A.,  
520 2012. Decadal scale variability of sea surface temperature in the Mediterranean Sea in relation to  
521 atmospheric variability. *Ocean Dyn.* 62, 13-30.

522 Steinhilber, F., Abreu, J.A., Beer, J., Brunner, I., Christl, M., Fischer, H., Heikkilä, U., Kubik, P.W.,  
523 Mann, M., McCracken, K.G., Miller, H., Oerter, H., Wilhelms, F., 2012. 9,400 years of cosmic  
524 radiation and solar activity from ice cores and tree rings. *Proceedings of the National Academy of*  
525 *Sciences* 109, 5967-5971, doi:10.1073/pnas.1118965109.

526 Stuiver, M., Reimer, P.J., 1993. Extended 14C database and revised CALIB 3.0 14C age calibration  
527 program. *Radiocarbon*, 35, 215-230.

528 Ternois, Y., Sicre, M.-A., Boireau, A., Marty, J.-C., Miquel, J.-C., 1996. Production pattern of  
529 alkenones in the Mediterranean Sea. *Geophys. Res. Lett.* 23, 3171-3174.

530 Trouet, V., Esper, J., Graham, N.E., Baker, A., Scourse, J.D., Frank, D.C., 2009. Persistent Positive  
531 North Atlantic Oscillation Mode Dominated the Medieval Climate Anomaly. *Science* 324, 78-80.

532

533

### Figure captions

534 Fig. 1. Map showing the location of Gol-Ho1B\_KSGC-31 site, and spatial field of  
535 Mediterranean annual mean SSTs (1955-2012). The insert in the upper right corner shows the  
536 monthly SSTs at the core location; the dashed line indicates the annual mean (17°C) from  
537 World Ocean Atlas Database (NOAA/NODC WOA13 (1° grid)). The anticyclonic blocking  
538 cell over the northeastern Atlantic and low-pressure system in the central Mediterranean  
539 associated to EA is also represented (adapted from Papadopoulos et al., 2012). All sites  
540 discussed in the text are shown from West to East: RAPiD-17-5P, South of Iceland (Moffa-  
541 Sanchez et al., 2014); MD99-2275, North of Iceland (Sicre et al., 2011); TTR17-1\_384B,  
542 436B, Alboran basin (Nieto-Moreno et al., 2013); MINMC-1,2, Balearic basin (Moreno et al.,  
543 2012). Mistral wind is shown by the black arrow.

544 Fig. 2. KSGC31 gravity core chronology based on  $^{210}\text{Pb}$  (grey dots) and  $^{14}\text{C}$  (dark squares)  
545 dating and associated error bar at  $\pm 1\sigma$  (A). The insert B is an enlarged view of the uppermost  
546 0-30 cm section of the core corresponding to the grey area. The outlier date shown as an  
547 empty square was not used in the age model.

548 Fig. 3.  $^{232}\text{Th}$  (A),  $^{210}\text{Pb}_{\text{xs}}$  (B) and  $^{137}\text{Cs}$  (C) profiles determined in the multicore Gol-Ho1B  
549 (dark dots) and gravity core KSGC31 (red squares) (see data in Table 2). KSGC31 profiles  
550 have been shifted to meet the best correspondence of the plots, yielding a material loss of  $15 \pm$   
551  $0.5$  cm in the top of the gravity core. Chronology of the multicore Gol-Ho1B and the top 10  
552 cm of the gravity core KSGC31 after adjustment based on  $^{210}\text{Pb}$  dating and associated age  
553 model uncertainty at  $\pm 1\sigma$  (D).

554 Fig. 4. SST reconstruction since 1850 AD combining SSTs from the multi-core Gol-Ho1B  
555 (light green dashed line and solid dots) and gravity core KSGC-31 (dark green and solid dots).  
556 Empty dots indicate the overlapping gravity core SST values with the multicore (A). Spliced  
557 Gol-Ho1B\_KSGC-31 record built from the two core data (B) (see text for explanations).

558 Fig. 5. Alkenone-derived SST reconstruction at the Gol-Ho1B\_KSGC-31 site over the  
559 instrumental period (A).  $^{14}\text{C}$  and  $^{210}\text{Pb}$  error bars on dating are shown for each SST data point.  
560 Kaplan instrumental data from 1866 AD to 2012 AD showing annual mean (in purple)(B),  
561 FMA months (in blue)(C) (Kaplan et al., 1998). Annual mean values of the East Atlantic (EA)  
562 index since 1950 are also shown for comparison with proxy data (D).

563 Fig. 6. Alkenone-SST time series from the Western Mediterranean Sea and North Atlantic  
564 over the last two millennia. (A) core Gol-Ho1B\_KSGC-31 (NW Mediterranean Sea) (this  
565 study); (B) Cores TTR17-1\_384B, 436B from the Alboran basin (Nieto-Moreno et al., 2013);  
566 (C) Cores MINMC-1,2 from the Balearic isles (Moreno et al., 2012); (D) core MD99-2275  
567 off North Iceland (Sicre et al., 2011). For (B) and (C) SSTs were recalculated using the  
568 calibration of Conte et al. (2006). Dashed lines in (C) highlight the portion of the record that  
569 has been extrapolated to present day from the last dated sediment horizon around 1500 AD  
570 (see text). Filled areas of the curves indicate negative SST anomaly relative to mean values of  
571 each core. A 25-yr binning was applied to all records (dark and red lines) to better visualize  
572 anomalies or departures from average conditions. Triangles indicate the AMS  $^{14}\text{C}$  control  
573 points for all cores. The grey vertical bars broadly highlight the most outstanding cold spells  
574 of core Gol-Ho1B\_KSGC-31 during the LIA. MCA: Medieval Climate Anomaly; LIA: Little  
575 Ice Age.

576 Fig. 7. A detailed view of the last millennium. (A) Fluctuations of the Great Aletsch and  
577 Gorner glaciers in the Swiss Alps (Holzhauser et al., 2005); (B) Retreat/advance of the  
578 Langjökull glacier (Iceland) reconstructed from the Hvítárvatn lake varves (Larsen et al.,  
579 2013; Ólafsdóttir et al., 2013); (C) Sea ice occurrence traced by the IP25 abundances (Massé  
580 et al., 2008) and alkenone-SSTs from core MD99-2275, North Iceland (Sicre et al., 2011); (D)  
581 Mg/Ca-SSTs obtained from foraminifera calcite of *G. inflata* in core RAPiD-17-5P, South  
582 Iceland (Moffa-Sanchez et al., 2014); (E) Alkenone-SSTs from site Gol-Ho1B\_KSGC-31 in  
583 the Gulf of Lion (this study); (F) 30-yr Gaussian low-pass filter of winter (DJF) European  
584 temperature anomaly (relative to the 1901 - 1995 calibration average) (black line) with two

585 standard errors (blue lines) (Luterbacher et al., 2004); (G) The NAO index anomalies  
586 calculated in 25-yr averages from the palæo-reconstruction by Ortega et al. (2015) (black  
587 line); 7-yr running average of the NAO instrumental (red line)  
588 ([http://www.esrl.noaa.gov/psd/gcos\\_wgsp/Timeseries/NAO/nao.long.data](http://www.esrl.noaa.gov/psd/gcos_wgsp/Timeseries/NAO/nao.long.data)). (H) Solar activity  
589 anomalies in  $\text{W/m}^2$  (Total Solar Irradiance, TSI) calculated in 25-yr averages from the cosmic  
590 ray intensity reconstruction (Steinhilber et al., 2012). From (B) to (E) dark and red lines  
591 indicate a 25-yr binning. From (C) to (H) filled areas indicate negative anomaly relative to  
592 average values, except for (F) whose anomaly was calculated relative to the 1901-1995  
593 calibration interval. Triangles indicate the AMS- $^{14}\text{C}$  control points at  $1\sigma$  uncertainty. The grey  
594 vertical bars broadly highlight the major cold spells of the LIA period in the Gol-  
595 Ho1B\_KSGC-31 record.

Table 1. Radiocarbon dates and their calibrated ages along the KSGC31 sediment core. Results are reported with a 1 $\sigma$  uncertainty.

Depth (cm)	Calibration	Material	<sup>14</sup> C age	cal year BP	Year AD	$\pm 1\sigma$
5.5	Oxcal 4.2, NH zone 1 post bomb ages curve	<i>Bittium</i> sp.	420 $\pm$ 30	24 <sup>a</sup>	1926	60
11.5	Oxcal 4.2, NH zone 1 post bomb ages curve	<i>Tellina</i> sp.	430 $\pm$ 30	34 <sup>a</sup>	1916	60
18.5	CALIB 7.1, Marine13 curve (Reimer et al., 2013)	<i>Pecten</i> sp.	720 $\pm$ 40	380 <sup>b</sup>	1570	78
25.5	CALIB 7.1, Marine13 curve (Reimer et al., 2013)	<i>Venus</i> sp.	640 $\pm$ 30	235	1716	99.5
41.5	CALIB 7.1, Marine13 curve (Reimer et al., 2013)	<i>Pecten</i> sp.	700 $\pm$ 30	339	1611	79
52	CALIB 7.1, Marine13 curve (Reimer et al., 2013)	Indet. bivalve	960 $\pm$ 30	551	1399	59
71	CALIB 7.1, Marine13 curve (Reimer et al., 2013)	<i>Arca tetragona</i>	1340 $\pm$ 30	852	1099	80.5
110.5	CALIB 7.1, Marine13 curve (Reimer et al., 2013)	<i>Venus</i> sp.	1465 $\pm$ 30	992	958	85
185.5	CALIB 7.1, Marine13 curve (Reimer et al., 2013)	<i>Nucula</i> sp.	2235 $\pm$ 40	1806	145	99.5
252	CALIB 7.1, Marine13 curve (Reimer et al., 2013)	juvenile bivalve shells (ind.)	2940 $\pm$ 30	2676	-726	100.5

<sup>a</sup> KSGC-31 core top ages are derived from 210 Pb xs profile (see methods, Table 2)

<sup>b</sup> Reversal, not used for the interpolation

Depth (in cm)	$^{210}\text{Pb}_{\text{xs}}$ mBq g <sup>-1</sup>	$^{232}\text{Th}$ mBq g <sup>-1</sup>	$^{137}\text{Cs}$ mBq g <sup>-1</sup>	Age in years AD Mean
Multi-core GOL-HO-1-1-B				
0.5	72 ± 9	22 ± 1	3 ± 1	2012 ± 0
1.5				2010 ± 0
2.5	74 ± 9	22 ± 1	4 ± 1	2008 ± 1
3.5				2006 ± 1
4.5	73 ± 8	21 ± 1	4 ± 1	2003 ± 1
5.5	64 ± 8	22 ± 1	4 ± 1	2001 ± 1
6.5	58 ± 5	21 ± 1	4 ± 0	1998 ± 2
7.5				1996 ± 2
8.5	52 ± 5	23 ± 1	4 ± 0	1993 ± 2
9.5				1990 ± 2
10.5	45 ± 7	25 ± 1	4 ± 1	1987 ± 3
11.5				1985 ± 3
12.5	48 ± 5	23 ± 1	4 ± 0	1982 ± 3
13.5				1979 ± 4
14.5	27 ± 4	26 ± 1	4 ± 0	1976 ± 4
15.5	30 ± 5	25 ± 1	3 ± 0	1973 ± 4
16.5	32 ± 4	25 ± 1	3 ± 0	1970 ± 5
17.5				1967 ± 5
18.5	21 ± 4	28 ± 1	2 ± 0	1963 ± 5
Gravity core KS-GC-31				
0.5	28 ± 5	26 ± 1	3 ± 0	1971 ± 1
1.5				1965 ± 2
2.5	17 ± 6	28 ± 1	2 ± 1	1959 ± 3
3.5				1953 ± 5
4.5	21 ± 6	30 ± 1	2 ± 1	1946 ± 6
5.5	20 ± 6	29 ± 1	1 ± 1	1940 ± 8
6.5	14 ± 6	31 ± 1	1 ± 1	1934 ± 10
7.5	8 ± 5	29 ± 1	0 ± 1	1928 ± 11
8.5	5 ± 5	29 ± 1	0 ± 0	1922 ± 13

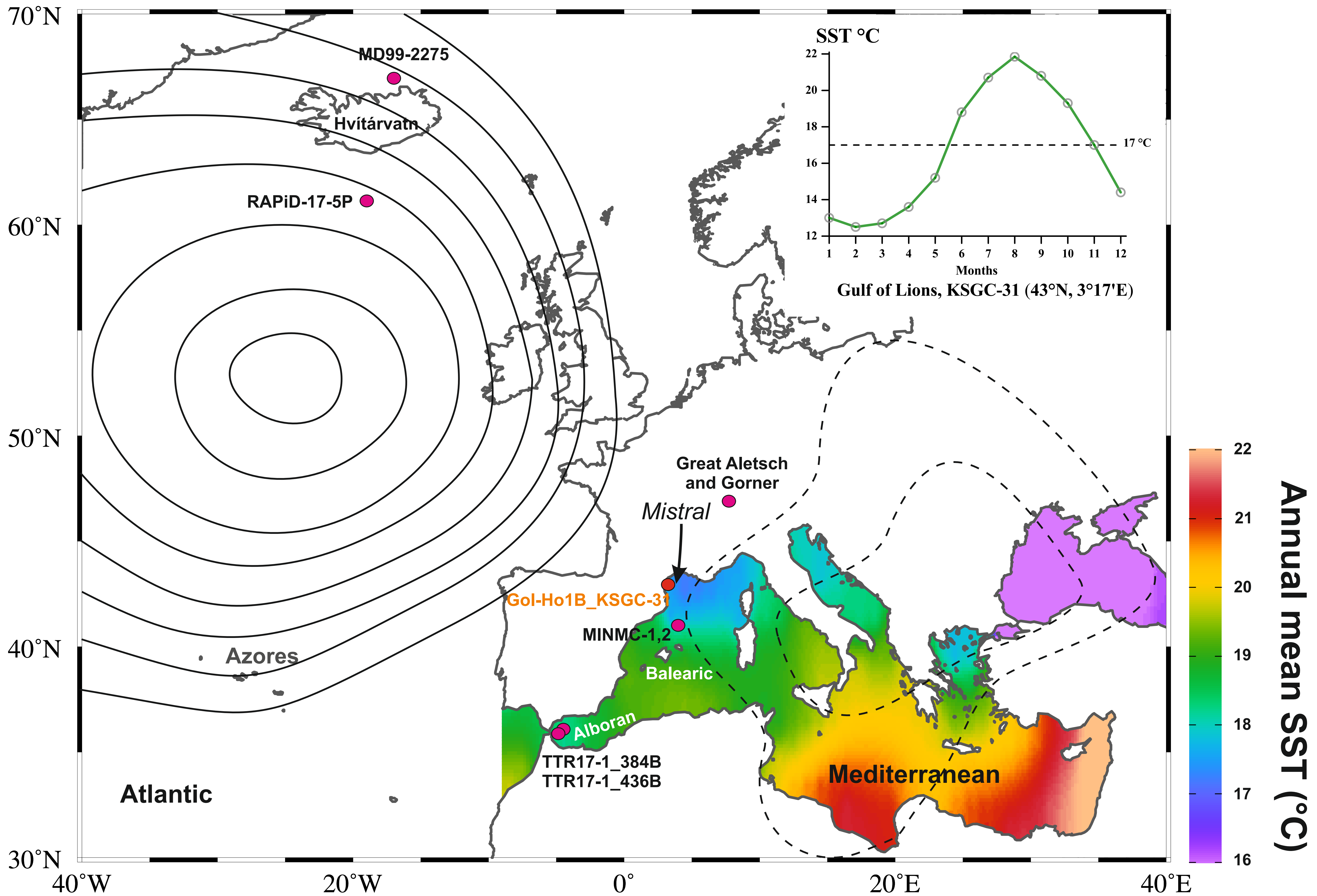


**Figure 1**

Age (years AD)

-1000

0

1000

2000

0

A/ Age:

---■---  $^{14}\text{C}$

●  $^{210}\text{Pb}$

50

100

150

200

250

Depth (cm)

B/ Zoom 0-30 cm

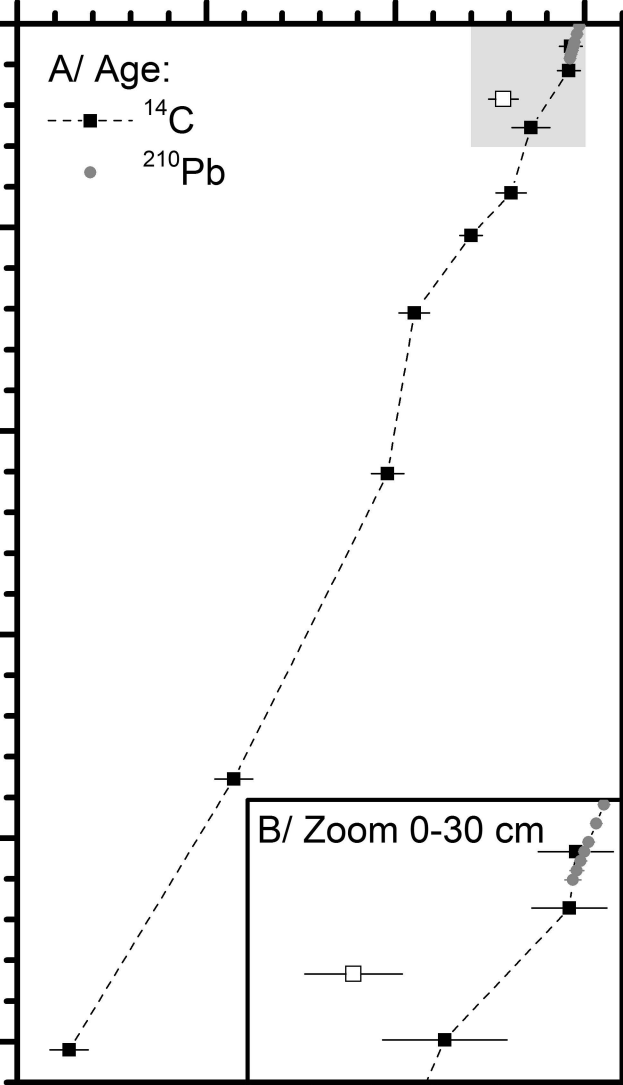
0

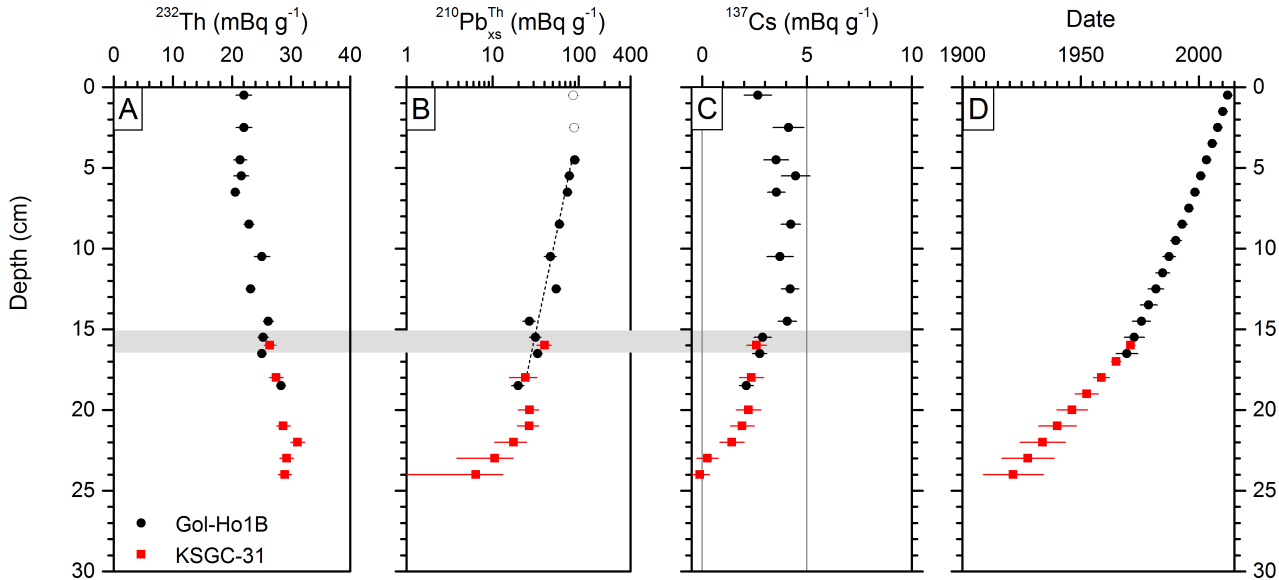
10

20

30

Depth (cm)





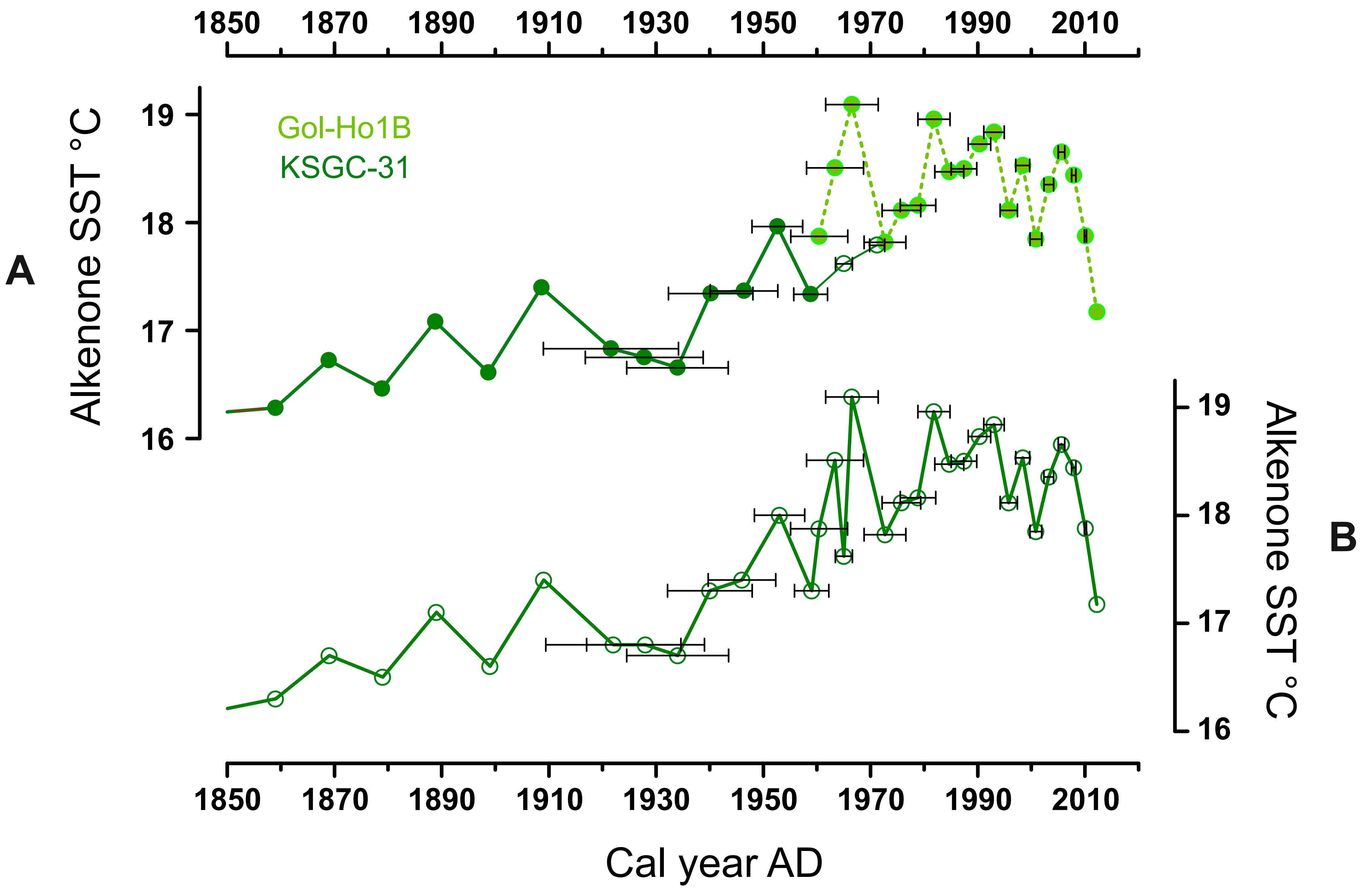


Figure 4

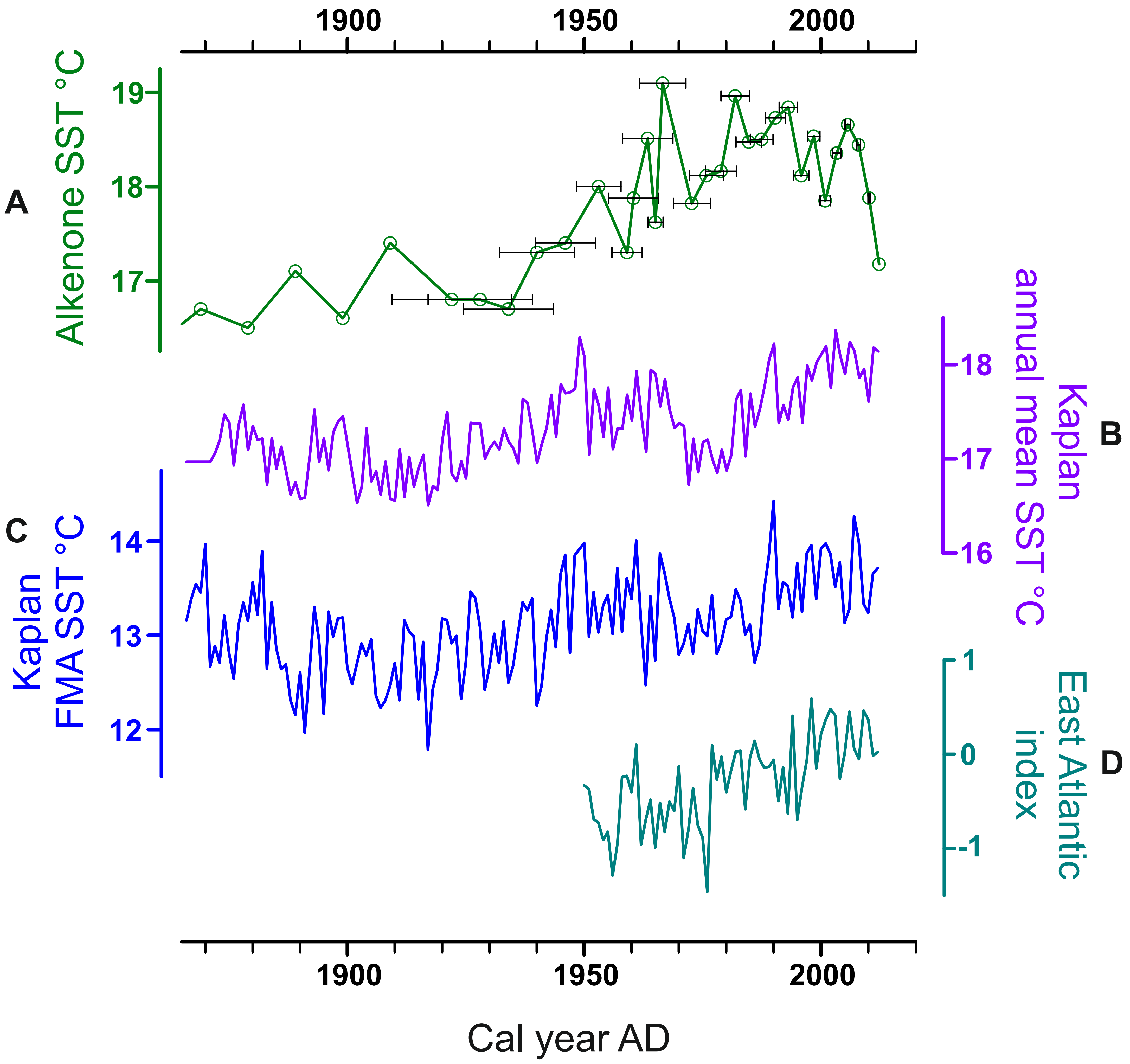


Figure 5

cal year AD

0 200 400 600 800 1000 1200 1400 1600 1800 2000

MCA

LIA

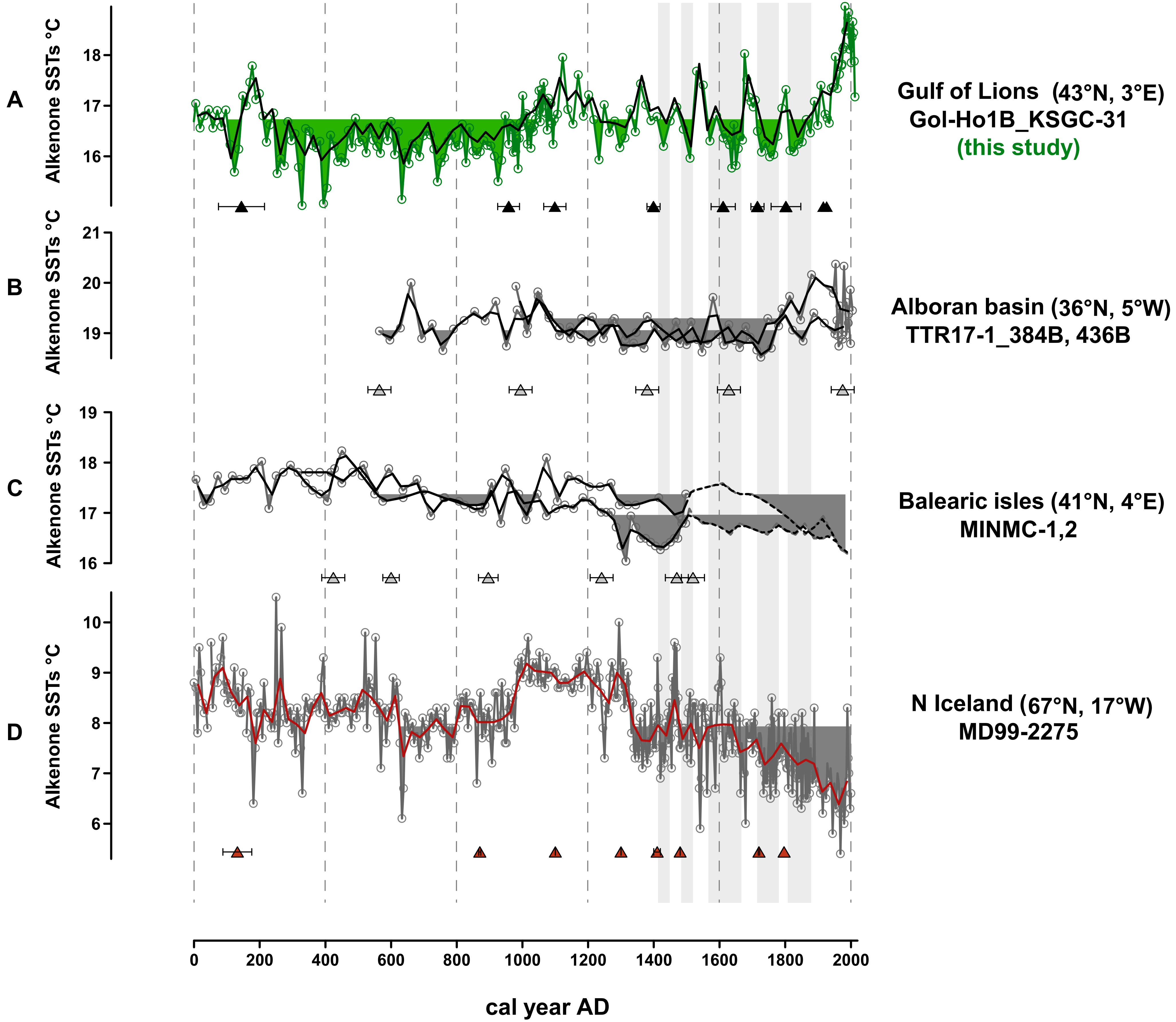


Figure 6

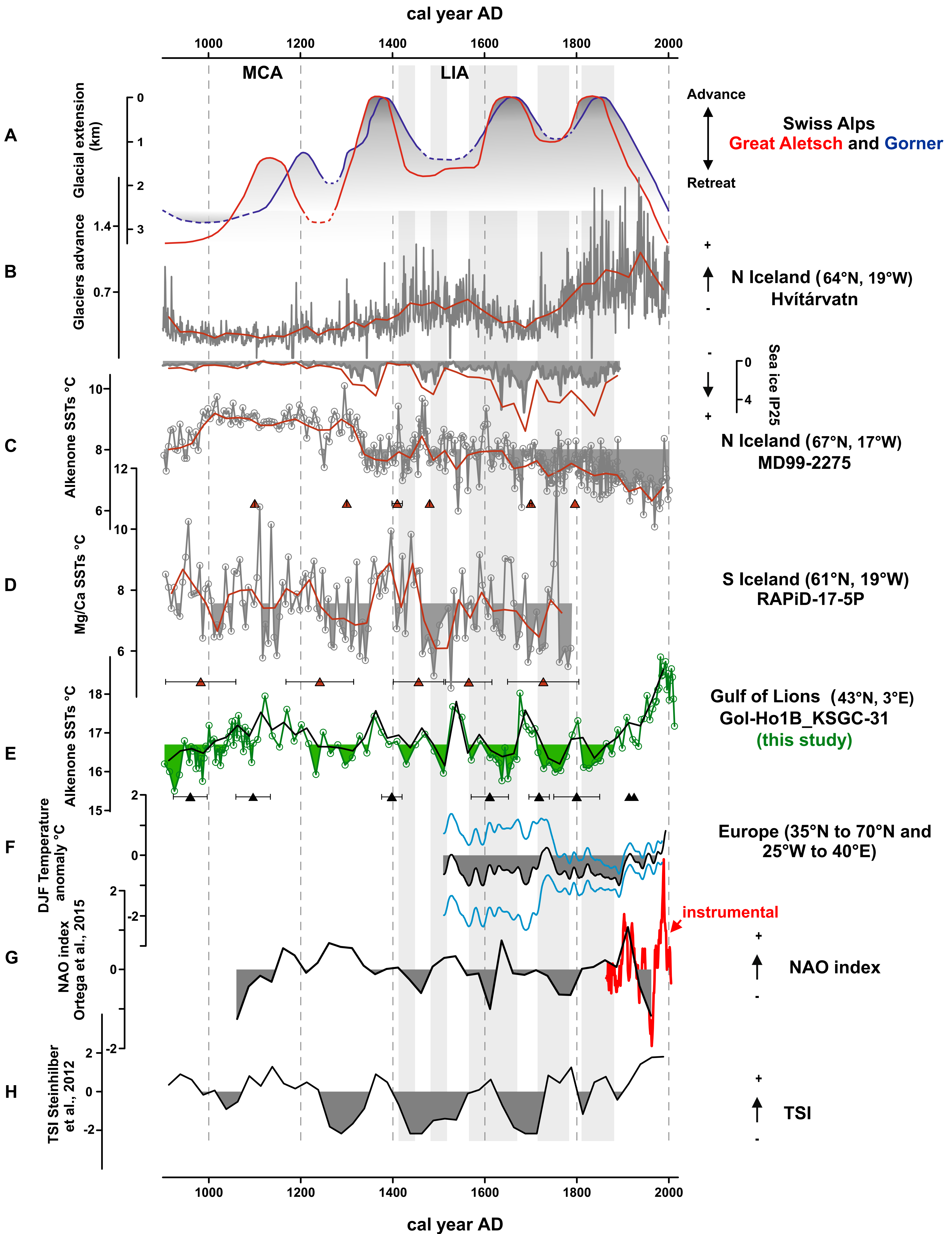


Figure 7